

Preparation of ZrB₂-MoSi₂ high oxygen resistant coating using nonequilibrium state powders by self-propagating high-temperature synthesis

Menglin ZHANG, Xuanru REN*, Mingcheng ZHANG, Songsong WANG, Li WANG, Qingqing YANG, Hongao CHU, Peizhong FENG*

School of Materials and Physics, China University of Mining and Technology, Xuzhou 221116, China

Received: January 30, 2020; Revised: March 31, 2021; Accepted: April 16, 2021

© The Author(s) 2021.

Abstract: To achieve high oxygen blocking structure of the ZrB₂-MoSi₂ coating applied on carbon structural material, ZrB₂-MoSi₂ coating was prepared by spark plasma sintering (SPS) method utilizing ZrB₂-MoSi₂ composite powders synthesized by self-propagating high-temperature synthesis (SHS) technique as raw materials. The oxygen blocking mechanism of the ZrB₂-MoSi₂ coatings at 1973 K was investigated. Compared with commercial powders, the coatings prepared by SHS powders exhibited superior density and inferior oxidation activity, which significantly heightened the structural oxygen blocking ability of the coatings in the active oxidation stage, thus characterizing higher oxidation protection efficiency. The rise of MoSi₂ content facilitated the dispersion of transition metal oxide nanocrystals (5–20 nm) in the SiO₂ glass layer and conduced to the increasing viscosity, thus strengthening the inerting impact of the compound glass layer in the inert oxidation stage. Nevertheless, the ZrB₂-40 vol%MoSi₂ coating sample prepared by SHS powders presented the lowest oxygen permeability of 0.3% and carbon loss rate of $0.29 \times 10^{-6} \text{ g} \cdot \text{cm}^{-2} \cdot \text{s}^{-1}$. Owing to the gradient oxygen partial pressure inside the coatings, the Si-depleted layer was developed under the compound glass layer, which brought about acute oxygen erosion.

Keywords: ZrB₂-MoSi₂ coatings; spark plasma sintering (SPS); high-temperature synthesis (SHS); active/inert oxidation; compound glass layer

1 Introduction

Carbon structural materials are widely exploited in aerospace high-temperature components, as indispensable structural materials in the national defense and civil fields, due to the low density, high specific strength,

excellent mechanical properties, and decent thermal shock resistance [1–5]. However, the characteristics of effortless oxidation above 673 K prominently constrain the application of carbon structural materials. Therefore, coating technology develops the best choice to heighten the high-temperature performance of carbon structural materials [6,7].

Of the field of oxidation resistance coatings in recent years, ZrB₂-based systems have been widely studied owe to their high melting point, low density, high thermal conductivity, and high strength at ultra-high

* Corresponding authors.

E-mail: X. Ren, XuanruRen@163.com;

P. Feng, fengroad@163.com

temperature [8–10]. However, ZrB_2 is challenging to achieve densification due to its strong covalent bond and low diffusion coefficient [11,12], which would also become porous during the oxidation process [13]. To suppress such defects, $MoSi_2$, the most commonly used sintering additive, was generally used to increase the compactness of ZrB_2 [14,15]. Moreover, the excellent film-forming properties of $MoSi_2$ can effectively reduce the oxidation consumption of ZrB_2 , thus making the ZrB_2 - $MoSi_2$ coating present great potential [16–18]. Recently, pressureless sintering methods are adopted to prepare the ZrB_2 - $MoSi_2$ coatings, exhibiting great potential. Jiang *et al.* [18] successfully prepared ZrB_2 - $MoSi_2$ -SiC-Si coating on graphite matrix by slurry dipping and vapor silicon infiltration methods. After oxidation at 1873 K for 150 h, the mass loss of the coating sample was only 0.21%. Yao *et al.* [19] used two-step pack cementation method to prepare SiC/SiC- $MoSi_2$ - ZrB_2 coating on C/C composites, and the weight loss after oxidation at 1773 K for 510 h was 0.5%. Zhang *et al.* [20] prepared ZrB_2 - $MoSi_2$ /SiC coating on C/C composites by combining the pack cementation method and the slurry painting method. After oxidation at 1273 and 1773 K for 30 and 10 h, the weight loss rates of the samples were 5.3% and 3.0%, respectively. Nevertheless, pressureless sintering generally requires ultra-high sintering temperature (above 2200 K) to achieve densification, which will lead to the generation of coarse grains, thereby weakening the oxidation resistance of the coatings.

Considering the oxidation protection of the coatings is a dynamic process, the structural oxygen blocking ability of the coating itself and the inert oxygen blocking ability of the self-generated compound glass layer constitute the oxidation protection of the coating for carbon matrix. In our previous work, we have found that the dispersion of Zr-oxides in the Zr-Si-B-O compound glass layer would strengthen the oxidation protection effect of the coating [21]. Nonetheless, for the ZrB_2 - $MoSi_2$ coatings, the by-products B_2O_3 and MoO_3 have intense volatility, and abundant gas volatilization will inevitably destroy the stability of the compound glass layer. Thus, it is necessary to improve the dynamic oxygen blocking ability of the ZrB_2 - $MoSi_2$ coating by constructing high oxygen resistant coating structure of the coatings. However, little work has been reported about the construction of ZrB_2 - $MoSi_2$ high oxygen blocking coating structure.

To improve the structural oxygen blocking ability of the coating, it is necessary to develop densification sintering technique at a lower temperature [22]. Spark plasma sintering (SPS) is well known as the low-temperature pressured rapid sintering technology, which can remarkably inhibit grain growth as well as bringing high density under pressure conditions [23–25]. In our previous work, HfB_2 -SiC-TaSi₂ coating [22] and ZrB_2 -SiC coating [13] have been prepared by SPS technology, both of which reveal excellent high-temperature oxidation resistance.

Utilizing high activity powders to improve the sintering performance is another way to enhance the structural oxygen blocking ability of the coatings. Recently, self-propagating high-temperature synthesis (SHS) method has been widely exploited in the preparation of composites [26–30], which has superior heating and cooling rates, being conducive to generate high activity due to the concentration of defects and non-equilibrium phases in the products. Iatsyuk *et al.* [28] used SHS method to prepare ZrB_2 -SiC ceramics with fine grains and high density. The porosity was only 1.5%, and the Vickers hardness was 24.3–25.0 GPa. Licheri *et al.* [31] prepared 40 vol% ZrB_2 -12 vol%ZrC-SiC composites by SHS method, with a relative density of 99.5%, the Vickers hardness of 16.9 ± 0.2 GPa, and the fracture toughness of 5.9 ± 0.5 MPa·m^{1/2}.

Although the combination of SPS and SHS methods to prepare ZrB_2 - $MoSi_2$ high oxygen resistant coating exhibits much potential, little work has been reported. Furthermore, the inhibition mechanism of the ZrB_2 - $MoSi_2$ coating for penetration of oxygen is still not clear, which can be used to fundamentally regulate the coating structure to obtain better oxygen blocking effect. Therefore, in this paper, ZrB_2 - $MoSi_2$ composite powders were first prepared by SHS technique, using which ZrB_2 - $MoSi_2$ coatings were prepared on graphite matrix by SPS technique. To avoid the interference of matrix oxidation consumption and reflect the authentic law of protection of the ZrB_2 - $MoSi_2$ coatings, graphite samples, coating standard samples, and coating samples were prepared simultaneously. Furthermore, the oxygen blocking ability of the ZrB_2 - $MoSi_2$ coatings prepared by SHS and commercial powders (CP) was quantitatively compared at 1973 K. The microstructure and forming mechanism of the self-generated compound glass layer were also further analyzed.

2 Experimental

2.1 Synthesis of ZrB₂–MoSi₂ powders by SHS

In this experiment, Zr (48 μm, 99.9% purity), B (1–3 μm, 95% purity), Mo (1–3 μm, 99.95% purity), and Si (1–3 μm, 99.9% purity) powders were used to prepare ZrB₂–MoSi₂ composite powders by SHS technique, which were manufactured by Beijing Licheng Innovation Metal Materials Technology Co., Ltd., China. In order to explore the influence of MoSi₂ content on oxygen blocking of the coatings, three components were designed, which were 60 vol%ZrB₂–40 vol%MoSi₂ (ZM40), 70 vol%ZrB₂–30 vol%MoSi₂ (ZM30), and 80 vol%ZrB₂–20 vol%MoSi₂ (ZM20). To guarantee the accurate phase contents of ZrB₂–MoSi₂ composite powders, we designed the content of the original powders according to the volume ratio of ZrB₂ and MoSi₂. Primarily, the weighed powders were put into ball mill with the ball-to-powder weight ratio of 5:1, which were milled at 300 r/min for 5 h. The mixed powders were dried in an oven at 333 K for 12 h. Subsequently, the dried powders were cold-pressed into a cylinder of 16 mm × 20 mm at a pressure of 200 MPa for 90 s. Afterward, the pressed sample was placed on the sample table of self-propagating reactor, whose upper surface was closely attached with molybdenum wire. Moreover, the reactor was vacuumized before introducing Ar gas as protective gas. After the protective gas was filled, the voltage regulating system applied current to the molybdenum wire, and then gradually preheated the sample until the self-propagating reaction occurred. When the combustion began, the voltage was turned off immediately until the self-propagation reaction of the sample was completed. Lastly, the composite powders obtained after combustion were crushed and grounded for 1 h, and then placed in a 333 K oven to dry for 12 h.

2.2 Sample preparation

To compare the difference in oxidation resistance between CP and SHS powders, ceramic samples (ϕ 12 mm) and coating samples (ϕ 15 mm) of ZM20–ZM40 were prepared by SPS furnace (Labox-125, Sinter Land Inc., Japan). The sintering temperature, pressure, heating rate, and holding time were 1773 K, 30 MPa, 180 K/min, and 5 min, respectively. The size of graphite matrix was Φ 12 mm × 2.5 mm, and the density was 1.6 g/cm³. ZrB₂ (1–3 μm, 99.9% purity) and MoSi₂ (1–3 μm, 99.9% purity) of CP were also manufactured by Beijing Licheng Innovation Metal Materials

Technology Co., Ltd., China. After SPS sintering, the graphite paper on the surface of the sample was polished clean with sandpaper to avoid data inaccuracy caused by the loss of graphite paper during the oxidation process.

2.3 Oxidation tests and microstructure characterization

The isothermal temperature oxidation test was carried out in a resistance furnace (SGMM4/19AE, Luoyang, China) at 1973 K. During the oxidation process, the analytical balance with sensitivity of 0.1 mg was utilized to weigh the crucibles containing the samples, and the oxidation kinetics, permeability, and protection efficiency of coatings and coating standard samples were further explored through the change of sample weight. Moreover, X-ray diffraction analysis (XRD, Bruker D8 ADVANCE XRD, BRUKER AXS, Germany) was used to detect the phase of the surface, an scanning electron microscope (SEM, FEI Quanta 250, FEI, USA) was exploited to analyze the microstructure, and its corresponding energy dispersive spectrometer (EDS, FEI Quanta 250, USA) scrutinized the composition and distribution of the phase, electron probe X-ray microanalysis (EPMA-8050G, SHIMADZU, Japan) was used for accurate qualitative analysis of the element distribution, and the transmission electron microscope (TEM, Tecnai G2 F20, FEI, USA) was utilized to evaluate the phase structure of the powders synthesized by the SHS technique. The cross-section backscatter SEM and cross-section EPMA samples were polished by SiC sandpapers with various specifications (100, 400, 800, and 1200 mesh), then ultrasonically cleaned with ethanol and placed in a 333 K oven to dry for 2 h.

2.4 Evaluation of oxygen blocking ability

To quantitatively evaluate the antioxidant capacity of the ZrB₂–MoSi₂ system, based on our previous work [22], Eqs. (1)–(6) characterized the dynamic protection process of the coatings in various oxidation stages.

$$\Delta M = \alpha_a T^{1/2} + C \quad (1)$$

where α_a represents the active factor, ΔM is the change of sample weight, T is the oxidation time, and C is a constant.

$$\eta = \frac{(m_{p,0} - m_{p,j}) - [(m_{s,j} - m_{s,0}) - (m_{c,j} - m_{c,0})]}{m_{p,0} - m_{p,j}} \times 100\% \quad (2)$$

$$\alpha_s = \frac{1}{n} \sum_{j=1}^n \frac{(m_{s,j} - m_{s,0}) - (m_{c,j} - m_{c,0})}{m_{p,0} - m_{p,j}} \quad (3)$$

$$\alpha_i = \frac{1}{n-4} \sum_{j=5}^n \frac{(m_{s,j} - m_{s,j-1})}{t} \quad (4)$$

where η represents the protective efficiency; α_s is the structure factor; α_i is the inerting factor; $m_{p,j}$, $m_{s,j}$, and $m_{c,j}$ are the weight gain per unit area of pure graphite, coating standard sample, and coating sample at j times of weighing, respectively; and t is the weighing interval ($t = 10$ min).

$$V_g = \frac{1}{n-3} \sum_{j=4}^n \frac{(m_{s,j} - m_{s,0}) - (m_{c,j} - m_{c,0})}{jt} \quad (5)$$

$$P = \frac{1}{n-3} \sum_{j=4}^n \frac{(V_{c,j} - V_{s,j})}{V_{p,j}} \times 100\% \quad (6)$$

where V_g is the carbon loss rate; P is the oxygen permeability; $V_{c,j}$, $V_{s,j}$, and $V_{p,j}$ are the weight change rate of coating sample, coating standard sample, and graphite matrix in j times of weighing, respectively.

3 Results and discussion

3.1 Microstructure of ZrB₂–MoSi₂ powders and coating

Figure 1 shows the XRD patterns of ZrB₂–MoSi₂ composite powders with various components synthesized by SHS technique. The synthesized powders consist only of ZrB₂ (#89-3930) and MoSi₂ (#41-0612), and no residual elemental phase is found, which is similar to the self-purify characteristics of SHS process in high-temperature combustion [32].

Figure 2 indicates the TEM and EDS micrographs of pure coating standard samples sintered by SPS technique. It can be found by EDS spectrum that there

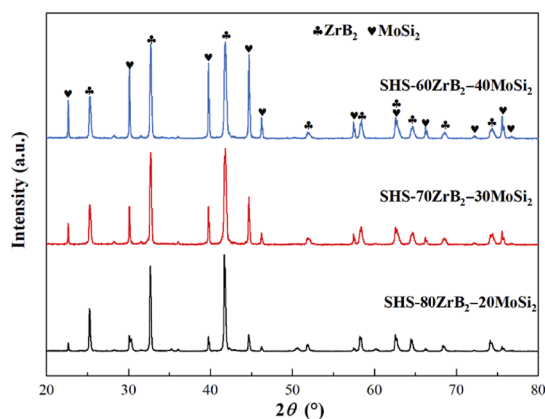


Fig. 1 XRD patterns of ZrB₂–MoSi₂ composite powders with various components synthesized by SHS technique.

are only ZrB₂ and MoSi₂ phases in the samples, which also proves that there is no phase transformation in the coating after SPS sintering. Furthermore, according to Fig. 2(a), the average grain size of the coating standard samples prepared by SHS powders after SPS sintering is merely 10–20 nm, further demonstrating that the SHS and SPS techniques can decrease the grain size and fine grain strengthening [33]. It can also be found from Fig. 2(b) that there is no noticeable phase interface between the various phases of the samples after sintering, which realizes superior metallurgical bonding.

In order to further characterize the bonding performance of coating and substrate before oxidation, the cross-section backscatter SEM micrographs of CP and SHS coating samples were compared in Fig. 3. It can be seen that CP-ZM20 component (Fig. 3(a)) has severe cracks after sintering, and noticeable loosening is found in its enlarged local diagram (Fig. 3(g)), which is related to the sintering characteristics of ZrB₂ [16]. Although SHS-ZM20 component also has a small number of microcracks (Fig. 3(b)), the phase structure after sintering is more compact than that of commercial powders. Additionally, with the increase of MoSi₂ content, superior metallurgical bonding is achieved between the coatings and the substrates, the various phases are evenly distributed, and there is no apparent aggregation phenomenon, especially the SHS-ZM40 component (Fig. 3(f)). This phenomenon is closely related to the sintering performance, which further

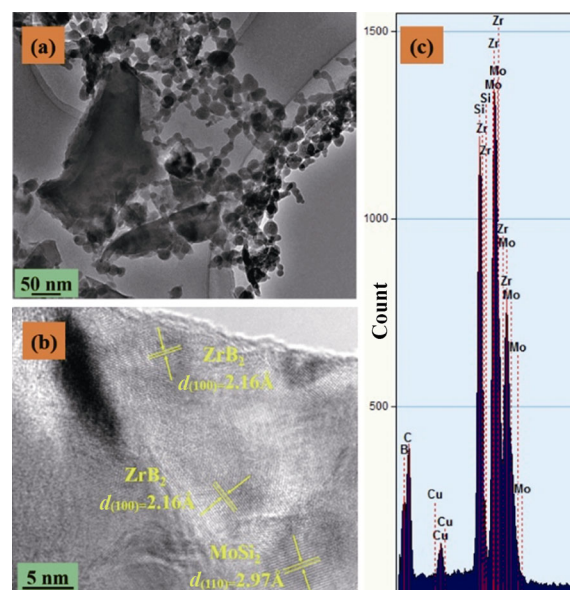


Fig. 2 (a, b) High-resolution TEM micrographs of SHS powders after sintering and (c) the corresponding EDS spectrum of (a).

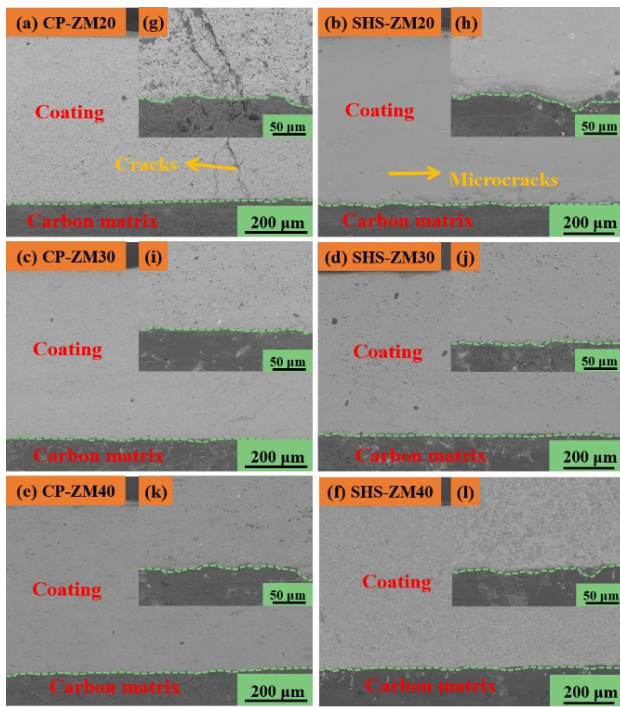


Fig. 3 Cross-section backscatter SEM micrographs of CP and SHS coating samples: (a, b) ZM20, (c, d) ZM30, (e, f) ZM40; and (g–l) are partial enlarged diagrams of (a–f).

verifies that the SHS synthesized powders have superior sintering activity.

3.2 Oxidation behavior comparison of SHS and CP coatings at 1973 K

In view of the interference caused by the oxidation loss of graphite matrix, the weight change of coating samples cannot reflect the actual law of protection. Therefore, the oxidation kinetics of SHS and CP coating standard samples at 1973 K were studied. Figures 4(a)–4(c) disclose the mass change curves of SHS and CP coating standard samples with various components after oxidation at 1973 K for 100 min. As can be seen from Fig. 4, the mass change curves of all component samples appear in parabolic form. Based on Eq. (1), after all curves are fitted by the parabola, we extract the active factor α_a of the samples, as shown in Fig. 4(d). It can be found that the active factor of both SHS and CP coating standard samples decreases with the growth of MoSi₂ content, which signifies that MoSi₂ can excellently constrain the oxidation of coatings. In addition, although the active factors of CP samples are the same as that of SHS samples, with the enhancement of MoSi₂ content,

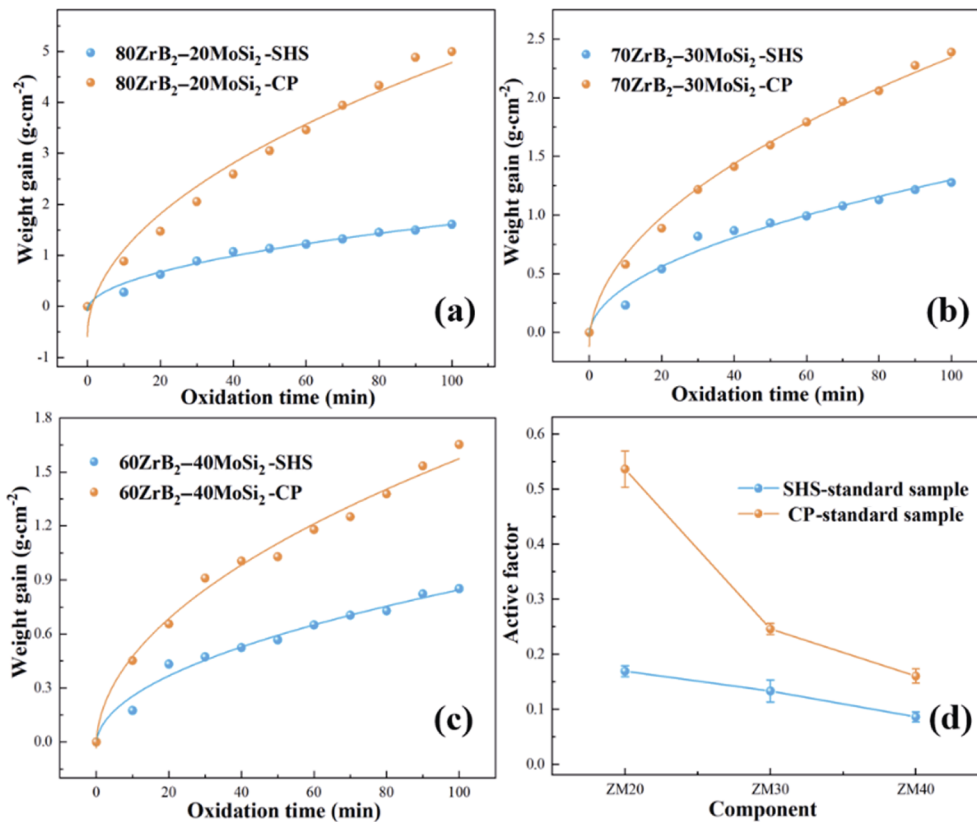


Fig. 4 (a–c) Weight change and curve fitting of SHS and CP coating standard samples after oxidation at 1973 K for 100 min; (d) active factors of SHS and CP coating standard samples with various components.

the active factor of SHS coating standard samples decreases from 0.537 to 0.170 (ZM20), 0.246 to 0.134 (ZM30), and 0.161 to 0.086 (ZM40) compared with CP coating standard samples, designating that SHS powders can efficiently diminish the oxidation activity of ZrB₂-MoSi₂ coating. The value of α_a manifests the oxidation resistance of the coating standard samples in the initial oxidation process. The smaller the α_a is, the more excellent the oxidation resistance of the coating itself is.

Figure 5(a) displays the weight gain rate curves of coating standard samples oxidized at 1973 K for 100 min. It can be seen from Fig. 5(a) that the weight of the samples first increases rapidly and then tends to be stable. In the active oxidation stage, the ZrB₂-MoSi₂ composite coating surface has not yet formed steady glass layer, which predominantly relies on the coating structure itself to block oxygen. With the prolongation of the oxidation time, the glass layer on the coating surface gradually forms and tends to be steady, and the oxidation enters the inert oxidation stage. At this time, the oxygen blocking is fulfilled by the joint action of the coating itself and the compound glass layer, in

which the oxidation rate of the coating would be significantly reduced. In order to scrutinize the impact of the reduction of oxidation activity on the protection ability, based on Eq. (2), we further investigate the oxidation protection efficiency of the coating with various components. As shown in Fig. 5(b), the protective efficiency of all the samples decreases first and then increases. This is mainly because, in the active oxidation stage, the suppression of oxygen by the coating is mainly achieved by its own structure. In contrast, in the inert oxidation stage, with the extension of oxidation time, the inhibition of oxygen by the coatings is significantly enhanced due to the formation of self-healing glass layer, thus expanding the oxidation protection efficiency of the coatings.

In addition, the inflection point of the oxidation protection efficiency curve of the CP coating appeared in about 10 min, while that of the SHS coating prepared with SHS powders appeared in 20–30 min. The prolongation of the turning point time is chiefly due to the significant decrease of the oxidation activity of the coatings prepared by SHS powders, which delays the formation of self-healing glass layer on the coating

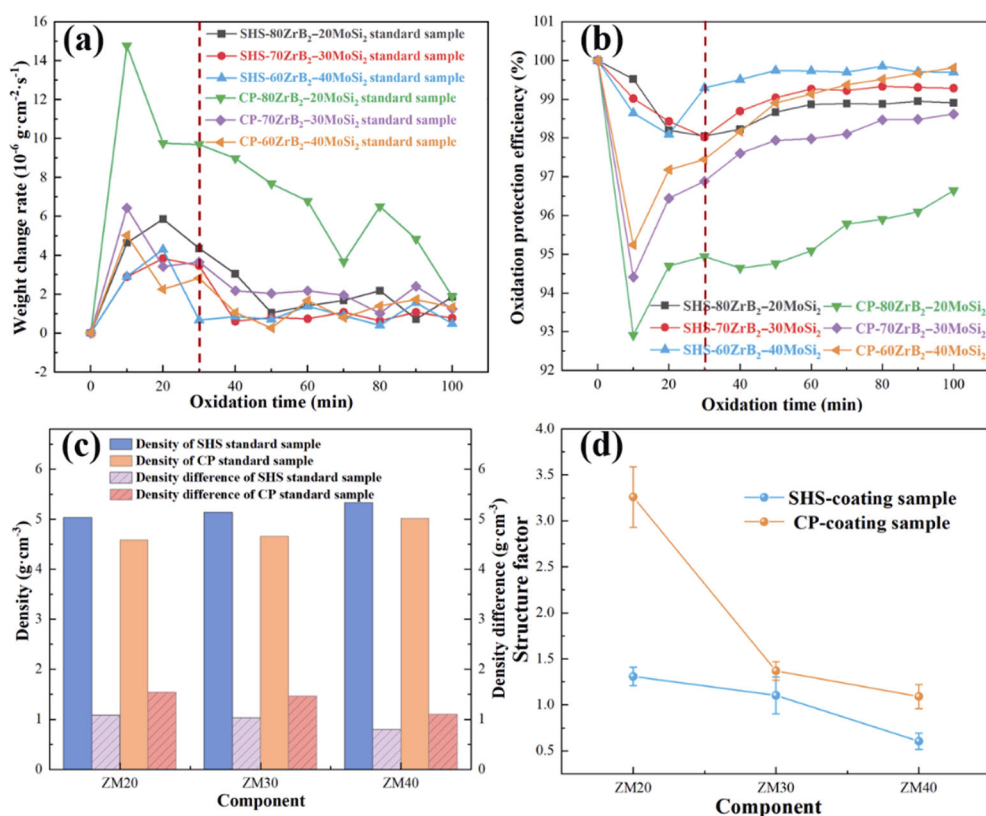


Fig. 5 (a) Weight gain curves of SHS and CP coating standard samples after oxidation at 1973 K for 100 min, (b) oxidation protection efficiency of SHS coating samples, (c) actual density and the difference value between the actual density and the theoretical density of SHS and CP coating samples, and (d) structure factors of SHS and CP coating standard samples.

surface. However, although the inflection point of oxidation protection efficiency of SHS coating appears late, the lowest value of oxidation protection efficiency at the inflection point is far higher than that of the CP coating. Figure 5(c) shows the density of coating samples with various components and the difference between the actual density and the theoretical density. As shown in Fig. 5(c), the density of SHS coating samples is higher than that of CP coating samples, and with the increase of MoSi₂ content, the difference between the actual density and the theoretical density gradually decreases, from 1.54 to 1.09 g/cm³ (ZM20), from 1.46 to 1.03 g/cm³ (ZM30), and from 1.10 to 0.79 g/cm³ (ZM40), respectively. Therefore, the improvement of coating density can effectively reduce the oxidation activity of coatings. Although it will delay the inflection point time, it can effectively improve the oxidation protection efficiency of the coating. Because of the close relationship between the enhancement of coating density and its structural oxygen blocking ability, based on Eq. (3), as shown in Fig. 5(d), we calculate the structure factor (α_s) to evaluate the oxygen blocking of the coating itself. The smaller the structure factor, the more solid the oxygen blocking of the coating structure. As can be seen from Fig. 5(d), the structure factors of all components of SHS coatings were lower than that of CP coatings, which decreased by 59.82% (ZM20), 20.44% (ZM30), and 44.95% (ZM40), respectively, indicating that the coating prepared by SHS powders could effectively heighten the structural oxygen blocking

ability of the coatings.

However, the stability of glass layer is also highly crucial as another oxygen blocking core in the inert oxidation stage. In order to avoid the distortion of the oxidation mechanism caused by internal matrix oxidation, the inert oxygen blocking ability of the glass layer is evaluated by coating standard samples. According to Eq. (4), the smaller the inerting factor, the greater the oxygen blocking of the glass layer. As seen from Fig. 6(a), with the increase of MoSi₂ content, both the inerting factors of coating standard samples prepared by CP and SHS powders diminish continuously, and the inerting factors of CP coating standard samples are significantly taller than those of SHS standard samples, revealing that the samples prepared by SHS powders have superior inerting ability.

With the intention of analyzing the effect of the surface glass layer on the inert oxygen blocking, Figs. 6(b)–6(g) show the cross-section backscatter SEM and EDS micrographs of various CP and SHS coating standard samples after oxidation at 1973 K for 100 min. Compared with the SHS components, CP coating standard samples exposed severe oxidation erosion, especially the CP-ZM20 component (Fig. 6(b)). There are large transverse cracks and evident loosening phenomena inside the samples. By comparing the distribution of O elements in the three components, the thickness of oxygen diffusion depth of CP-ZM20, CP-ZM30, and CP-ZM40 components reduces in turn, which are 345.6, 186.1, and 133.8 μm , respectively

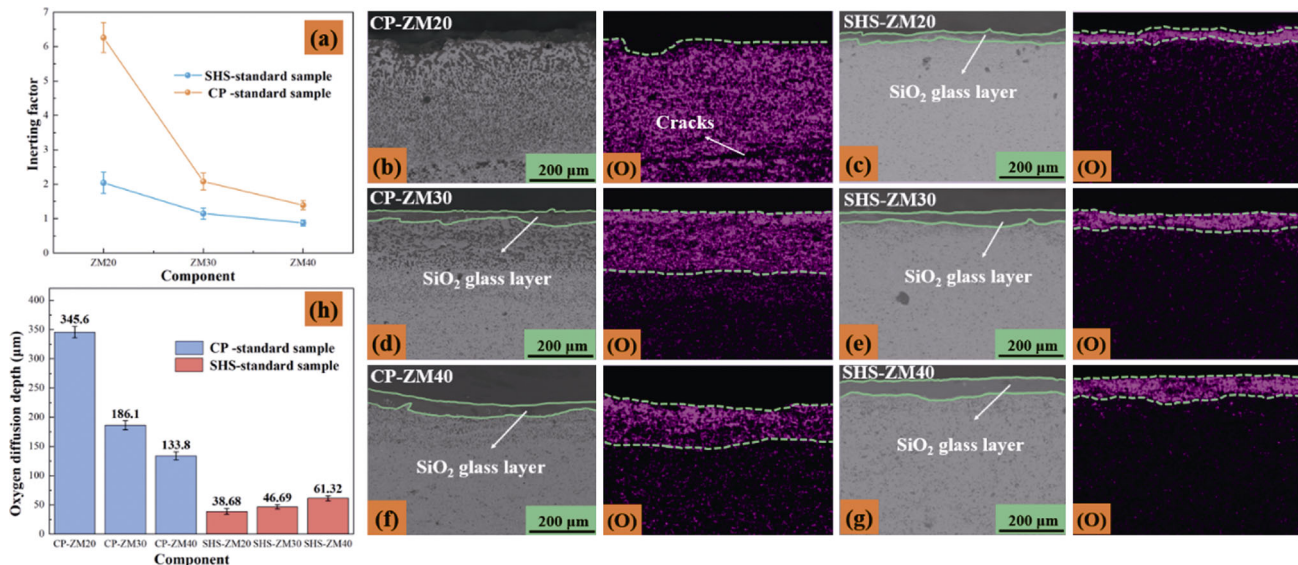


Fig. 6 (a) Inerting factor of CP and SHS coating standard samples with ZM20–ZM40 components, (b–g) cross-section backscatter SEM and EDS micrographs of CP and SHS coating standard samples after oxidation at 1973 K for 100 min, and (h) oxygen diffusion depth of CP and SHS coating standard samples after oxidation.

(Fig. 6(h)). However, for SHS components, there are no apparent crack, pore, or other defect after oxidation. The thicknesses of the oxygen diffusion depth enlarge with the increase of MoSi₂ content, which are 38.68, 46.69, and 61.32 μm, respectively. It is easy to spot that with the increase of MoSi₂ content, the diffusion depth of O element in CP samples decreases. This is because the antioxidant capacity of the coating depends to a large extent on the coating structure after the sintering. In Fig. 5(c), we have found that the density of sintered CP powders is lower than that of SHS powders, and the loose structure of low-density samples leads to the increase of oxygen diffusion depth and even obvious cracks (Fig. 6(b)). The increase of MoSi₂ content can expand the density of the samples, and form the thicker SiO₂ glass layer, which greatly limits the diffusion of oxygen in the interior. Nevertheless, for the SHS samples, the dense structure causes the oxygen blocking mechanism to shift from the structure to the component dominated. Because the components with high ZrB₂ content will produce more gas by-products due to oxidation, leading to the formation of more oxidation pores on the surface [12]. Meanwhile, the lower content of MoSi₂ leads to the lack of sufficient SiO₂ to pad these oxidation pores, resulting in a thinner glass layer. ZM40 component can rapidly shape steady SiO₂ glass layer at the same time owing to sufficient silicide and relatively low boride. When the oxygen diffusion is not severe, the increase of glass layer thickness enhances the stability of the samples. It shrinks the possibility of oxygen diffusion into the interior, and thus attains better oxygen blocking effect, which also clarifies why the SHS-ZM40 component in Fig. 6(a) exhibits the lowest inerting factor. Therefore, it is further confirmed that the SHS powders have lower oxidation activity than the CP powders at the ultra-high temperature of 1973 K.

In order to reveal the specific effect of the glass layer on the oxygen blocking process, Fig. 7 shows the XRD patterns of the SHS coating samples with various components after oxidation at 1973 K for 100 min. After oxidation, the ZrB₂ and MoSi₂ phases on the surface of the samples completely disappear, with only ZrO₂, SiO₂, MoB (#51-0940), ZrSiO₄ (#33-1485) phases present, and no obvious Mo₅Si₃ phase appears. ZrO₂ is dominated by monoclinic structure (#72-1669) and a small amount of tetragonal structure (#79-1768), which is consistent with Ref. [34]. Moreover, it can be easily observed from Fig. 7 that the peak of SiO₂ amorphous

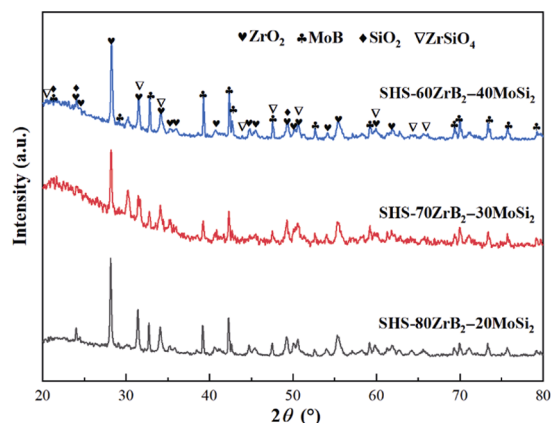
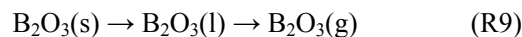
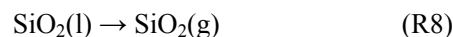
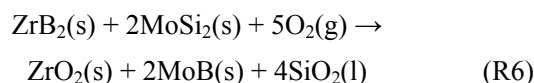
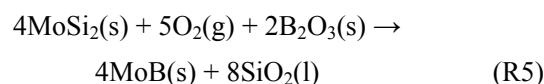
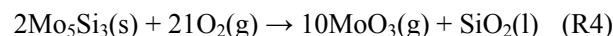


Fig. 7 XRD patterns of SHS coating samples after oxidation at 1973 K for 100 min.

state becomes more and more evident with the increase of MoSi₂ content. As we all known, MoO₃, as a by-product of MoSi₂, begins to volatilize at 923 K [35], while B₂O₃, due to its low melting point (723 K), also has intense volatility, especially at the ultra-high temperature of 1973 K, which clarifies why B₂O₃ and MoO₃ phases are not detected in XRD. The possible reactions in the oxidation process are shown in Eqs. (R1)–(R9) [35,36].



On the other hand, the film-forming quality of the compound glass layer on the coating surface is associated with the internal structure of the coatings and plays a crucial role in the high oxygen blocking system. Therefore, Fig. 8 describes the surface SEM micrographs of SHS and CP coating samples after oxidation at 1973 K for 100 min. Combined with XRD and EDS, it can be discovered that the black and gray phases are SiO₂, the white phases are ZrO₂, ZrSiO₄, and the bright white phases are MoB, which are dispersed in the glass layer on the surface.

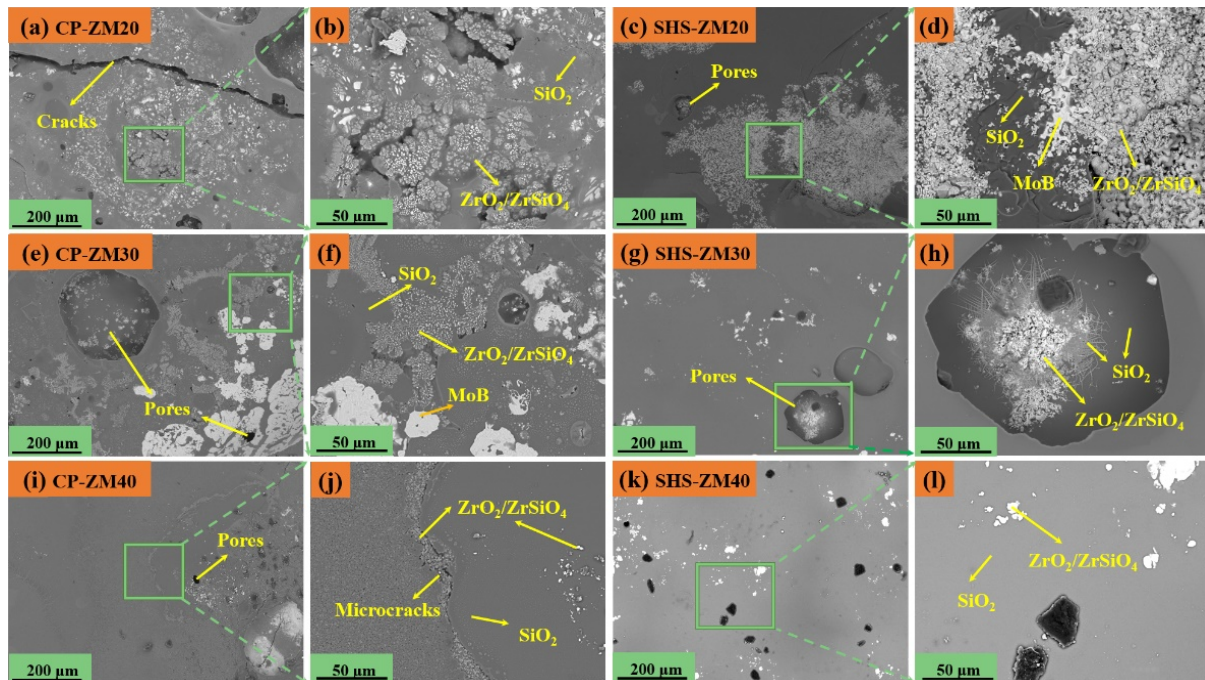


Fig. 8 Surface backscatter SEM micrographs of CP and SHS coating samples after oxidation at 1973 K for 100 min: (a–d) ZM20, (e–h) ZM30, and (i–l) ZM40.

As shown in Figs. 8(a)–8(d), scores of white oxides are dispersed on the surface of the ZM20 components. Based on its partial enlarged diagram, it can be detected that the oxides are not uniformly distributed, but appear local agglomeration phenomenon. The reason is that plenty of $ZrSiO_4$ and ZrO_2 are precipitated from the high content of ZrB_2 , the low content of silicide leads to the insufficient supply of SiO_2 glass on the surface, and the oxide particles cannot be homogeneously dispersed, resulting in the oxide agglomeration. Furthermore, the content of the gas by-product B_2O_3 will increase accordingly, and a large amount of pores appear in the coating, which provides diffusion channels for the infiltration of oxygen [37]. The CP-ZM20 (Figs. 8(a) and 8(b)) component has large cracks on the surface due to its higher oxidation activity, which also explains why the component in Fig. 5(b) shows the lowest oxidation protection efficiency.

However, the surface of the ZM40 coating sample (Figs. 8(i)–8(l)) tends to be flat, without obvious holes and cracks. With the increase of $MoSi_2$ content, the oxygen diffusion rate of oxidation product SiO_2 is relatively low [35]. At the ultra-high temperature of 1973 K, the pores caused by gas by-products are continuously filled with SiO_2 . Therefore, there is no obvious aggregation of Zr-oxides and Mo-oxides on the surface. Although there are a few unhealed microcracks

on the surface of the CP-ZM40 (Figs. 8(i) and 8(j)) component, compared with the component with low content of $MoSi_2$, the flatness of the surface can still characterize the outstanding stability of ZM40 components.

As shown in Figs. 8(e)–8(h), the white phases on the surface of ZM30 coating sample are appreciably reduced, and bulky holes are created simultaneously. Among them, the surface of CP-ZM30 formed significantly more white oxides than SHS-ZM30 coating sample, which is related to the coating structure after oxidation. It has been found in Fig. 6(c) that CP-ZM30 component has more severe oxygen erosion during the oxidation, giving rise to the breeding of a large amount of transition metal oxides. In addition, in the enlarged micrographs, it can also be found that there are lots of $ZrSiO_4$ and ZrO_2 in the pores, which indicates that the Zr-oxides may not only precipitate on the surface, but may be dispersed in the SiO_2 glass layer, thereby forming the compound glass layer with excellent oxygen blocking.

3.3 Oxygen blocking mechanism of coatings

To deeply analyze the structural changes of the coatings after oxidation, Fig. 9 shows the cross-section EPMA micrographs of SHS coating samples after oxidation at 1973 K for 100 min. Based on Fig. 9, the interior of the

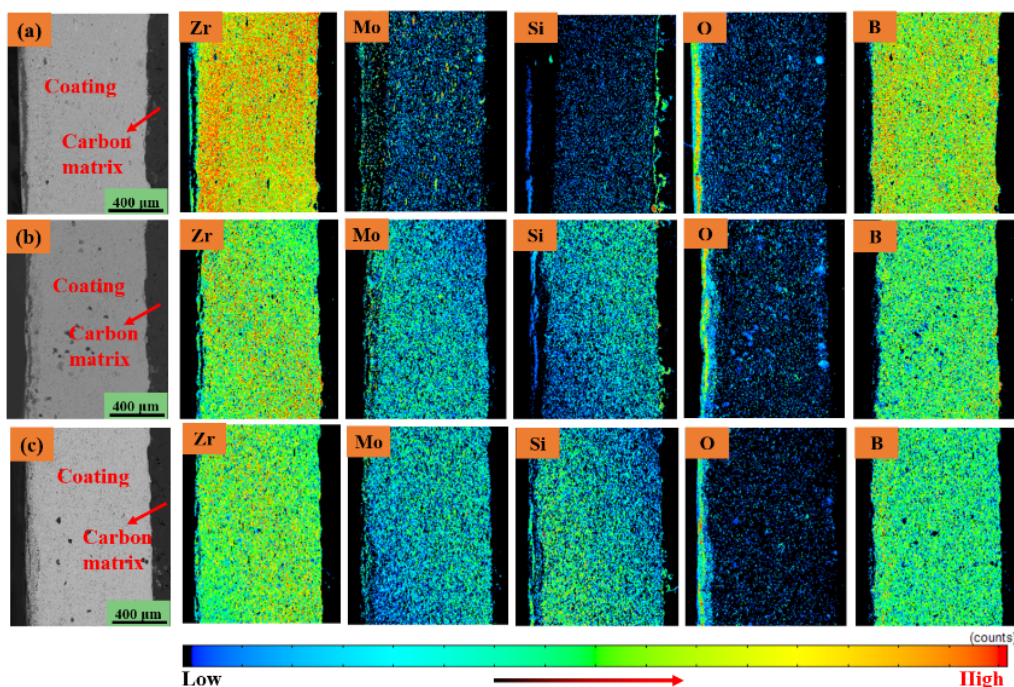


Fig. 9 Cross-section EPMA micrographs of SHS coating samples after oxidation at 1973 K for 100 min: (a) SHS-ZM20, (b) SHS-ZM30, and (c) SHS-ZM40.

coating is still dominated by ZrB_2 , and there are no penetrating cracks or large holes, indicating that the three coating samples of ZM20–ZM40 display excellent effects of blocking oxygen penetration at 1973 K. However, an interesting phenomenon is likewise discovered in the spectra of Si element, that is, all coating samples have the absence of Si elements under the glass layer, which is called Si-depleted layer. The Si-depleted layers of ZM20–ZM40 component coating samples are 165.7, 95.03, and 64.09 μm , respectively, which is the same as that of coating standard samples. In fact, Fahrenholtz [38] has proved that the appearance of the depletion layer is not only related to pressure and temperature, but also associated with the structure after sintering. Moreover, the SiO_2 glass is in molten state at 1973 K, the gas by-products of ZrB_2 and MoSi_2 will accelerate the flow inside the coating, the convection of liquid glass inside the coating will lead to the delamination in the oxidation region [24,39], and the low oxygen partial pressure in the coating will lead to the violent volatilization of silicon (Fig. 10(a)), resulting in the appearance of Si-depleted layers. In the interior of the coating samples, the O element penetration of the SHS-ZM20 component is supreme, which further verifies that the oxidation pores formed by high content of boride will turn into the channel of oxygen diffusion, resulting in generous oxygen penetration. With the

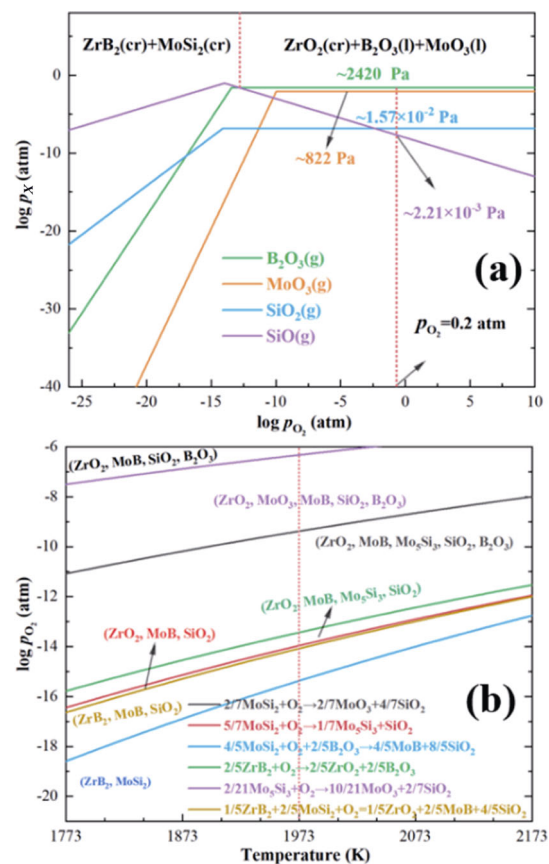


Fig. 10 (a) Volatile phase diagram of ZrB_2 – MoSi_2 coating at 1973 K and (b) oxygen partial pressure of Eqs. (R1)–(R6) at 1973 K.

increase of MoSi₂ content, the degree of oxygen penetration into the interior decreases in turn, establishing the relatively straightforward layer structure, which is consistent with the change of glass layer thickness in Fig. 6. It further confirms that the lower the inerting factor of the coating samples, the bigger the thickness of the glass layer, and the better the inert protection effect of the glass layer.

For the delamination phenomenon in EPMA micrographs (Fig. 9), the volatile phase generated during the oxidation process plays a crucial role. Consequently, according to the thermodynamic model constructed by Fahrenholtz [40] and the ZrB₂–SiC volatility diagram calculated by Kubota *et al.* [24], Fig. 10(a) plots the volatility diagram of volatile phases (MoO₃, B₂O₃, SiO₂, and SiO) that may exist in the oxidation process of coating samples at 1973 K; other secondary volatile phases (ZrO₂, MoB, etc.) have minor influence, and hence they are not taken into account [34], in which the thermodynamic data is provided by HSC chemistry software. Moreover, it can be seen from Fig. 10(a) that the vapor pressure of B₂O₃(g) in air is the tallest, 2420 Pa. And the vapor pressure of MoO₃(g) is 822 Pa, which is inferior to B₂O₃(g). The equilibrium vapor pressure of SiO₂(g) and SiO(g) is merely 1.57×10^{-2} and 2.21×10^{-3} Pa, respectively. Thus, when the oxidation enters the active oxidation stage, the oxygen partial pressure (p_{O_2}) inside the coating is approximately equal to the oxygen partial pressure in the air ($p_{O_2} = 0.2$ atm). No matter the coating surface or the interface between the coating and the substrate, the oxidation reaction will take place in varying degrees. At this time, the oxidation products MoO₃(g) and B₂O₃(g) in Eqs. (R1) and (R2) volatilize first. With the oxidation entering the inert oxidation stage, the well-sealed compound glass layer has been shaped on the surface, and both the volatilization of internal gas and the erosion of external oxygen have been efficaciously impeded, which makes the pressure inside the coating samples have observable gradient alteration, and the oxygen partial pressure from the coating surface to the inner matrix similarly demonstrates the phenomenon of gradual decrease.

Nonetheless, the boundary between diverse layers is the initial region of oxidation, and the oxygen partial pressure at equilibrium represents the necessary condition for oxidation, which determines the oxidation reaction sequence [23], and further reflects the change of coating structure. Consequently, the equilibrium

oxygen partial pressure of Eqs. (R1)–(R6) at 1973 K was calculated by HSC chemistry, as shown in Fig. 10(b). The equilibrium oxygen partial pressure of Eq. (R5) is minimum at 1973 K, which is only 5.01×10^{-16} atm, indicating that MoSi₂ preferentially oxidizes with B₂O₃ and O₂ to form MoB phase at low oxygen partial pressure [34], and Eq. (R6) is barely inferior to Eq. (R5). Furthermore, the simultaneous oxidation of ZrB₂ and MoSi₂ also preferentially forms stable MoB phase. While the Mo₅Si₃ phase in R3 can also be shaped at insufficient oxygen partial pressure, when it reaches the surface of the compound glass layer, the oxygen partial pressure is similar to air ($p_{O_2} = 0.2$ atm), and Mo₅Si₃ phase will continue to react with O₂ to generate MoO₃ volatile phase (Eq. (R4)). What is more, for the components with high boride content, due to the high oxidation activity of ZrB₂ and the lack of SiO₂ glass formation, extensive gas by-products are generated. In the volatilization process, the gas by-products convey the Si of the Si-depleted layer to the coating surface, bringing about the Si-depletion layer. With the rise of MoSi₂ content, the density of the coating enhances and the amount of gas by-products generated decrease, which also explains why the thickness of the Si-depleted layer is inversely proportional to MoSi₂ content in EPMA (Fig. 9), and only MoB phase is detected in XRD, but no other Mo-oxides are unearthed.

Figure 11 presents the high-resolution TEM micrographs of the surface glass layer of the SHS-ZM40 coating sample after oxidation at 1973 K for 100 min. Figure 11(b) is the partial enlarged diagram of Fig. 11(a). Substantial nanocrystalline particles are dispersed in the compound glass layer with a diameter of about 5–20 nm. TEM micrographs can further confirm in Figs. 11(c) and 11(d) that the oxides scattered in the glass layer are primarily ZrO₂ and ZrSiO₄. Although it is detected in Fig. 8(i) that white Zr-oxides precipitate on the surface, more Zr-oxides are embedded in the glass layer to establish steady compound glass layer.

However, in addition to the formation of stable compound glass layer on the surface, the focus of the high oxygen blocking system is the internal structure of the coating, which is the core determining whether the high oxygen blocking can be fulfilled. Figure 12 is the structure diagram of the ZrB₂–MoSi₂ coating samples after oxidation at 1973 K for 100 min. Figure 11(b) has proved that the compound glass layer is composed of ZrO₂ and ZrSiO₄ nanocrystalline particles dispersed in the molten SiO₂ glass, while ZrO₂ has merely one

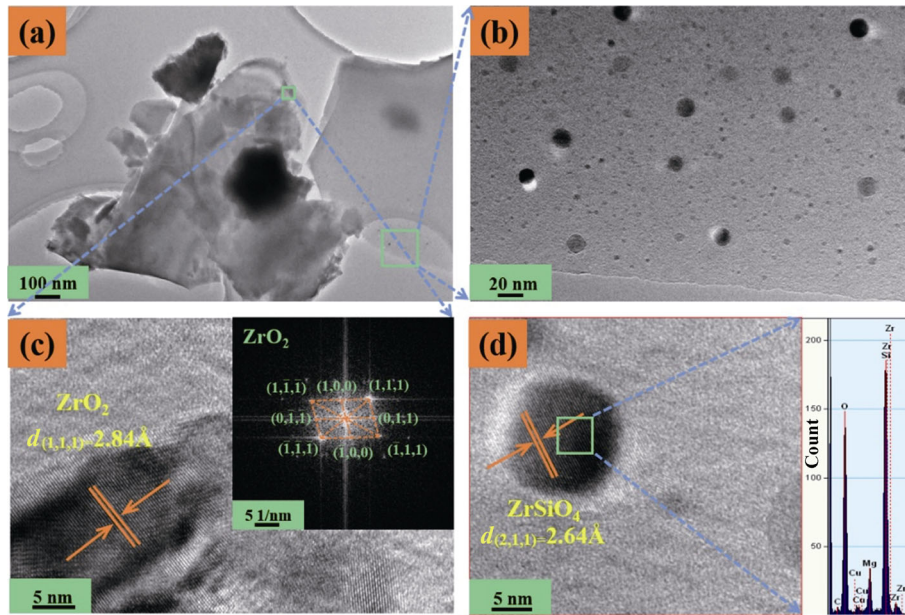


Fig. 11 (a) TEM micrographs of surface glass layer of SHS-ZM40 coating sample after oxidation at 1973 K for 100 min and (b–d) are partial enlarged diagrams of (a).

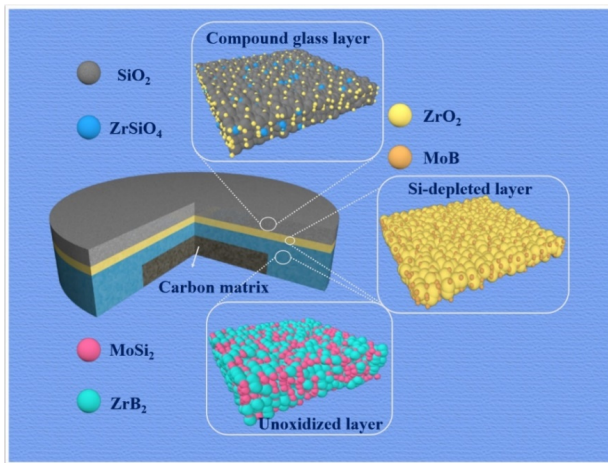


Fig. 12 Structure diagram of ZrB₂–MoSi₂ coating samples after oxidation at 1973 K for 100 min.

coordination number in the silicate glass, which is located in the cube [ZrO₈]. Due to the large ion radius, Zr⁴⁺ is mainly outside the structural network in silicate glass, and the higher melting points of ZrO₂ (2973 K) and ZrSiO₄ (2773 K) have good stability. However, the content of Zr-oxides is not as high as possible. SiO₂ glass exists in the form of [SiO₄], which is connected through “bridging oxygen” to form the three-dimensional structure. Excessive ZrO₂ content in the glass will cause [SiO₄] to slightly deform and tend to be compacted, and thus the molecular volume is reduced, the thermal expansion coefficient is expanded, and the phenomenon of oxide accumulation occurs.

It can be seen from Fig. 10 that although B₂O₃, the gas by-product of ZrB₂ oxidation, has intense volatility at 1973 K, MoSi₂ can react with it to produce MoB, as shown in Eq. (R3), thereby reducing the pressure difference triggered by the formation of oxidation pores in the coating, and thus reducing the possibility of oxygen penetrating the substrate. It can also be attained from the EPMA micrographs in Fig. 9 that the Si-depleted layer decreases with the enhancement of MoSi₂ content, and the internal oxidation of the coating declines accordingly. Furthermore, the decrease of B₂O₃ volatilization will correspondingly multiply the viscosity of the glass layer, hence avoiding the rapid migration of borosilicate glass due to low viscosity [34], and augmenting the stability of the compound glass layer.

However, to evaluate the oxidation resistance performance, only the structure and inerting factors are not enough. Fundamentally, the quantitative evaluation of the loss degree of the internal carbon matrix can truly manifest the oxygen blocking effect of the system. Therefore, this study calculates the carbon loss rate and oxygen permeability of the SHS and CP coating samples according to Eqs. (5) and (6), as shown in Fig. 13. The carbon loss rate of ZM20–ZM40 coatings prepared by SHS powders is 1.22×10^{-6} , 0.87×10^{-6} , and 0.29×10^{-6} g·cm⁻²·s⁻¹, and the oxygen permeability is 1.09%, 0.55%, and 0.30%, respectively. It can be further found from Fig. 13 that the oxygen permeability and carbon loss rate of the CP coating samples are higher than the

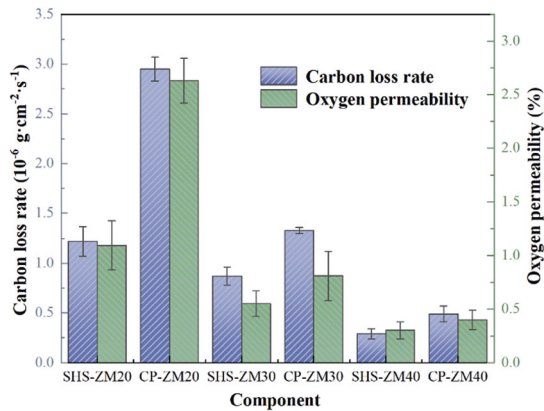


Fig. 13 Carbon loss rate–oxygen permeability curve of SHS and CP coating samples after oxidation at 1773 K for 100 min.

corresponding SHS coating samples. Furthermore, compared with SHS-ZM20 and SHS-ZM30, the carbon loss rate of SHS-ZM40 decreased by 76.2% and 66.7%, and the oxygen permeability decreased by 72.5% and 45.5%, respectively. This proves that the 60 vol% ZrB_2 –40 vol% MoSi_2 composite powders synthesized by SHS technique, after preparation of the coating, have decent resistance at 1773 K due to their lower oxidation activity and excellent structural stability.

4 Conclusions

SHS and SPS techniques were utilized to enhance oxygen blocking of ZrB_2 – MoSi_2 composite coatings under 1773 K aerobic environment. The ZrB_2 –40 vol% MoSi_2 coating sample prepared using SHS powders exhibits the best oxygen blocking ability at 1773 K. Compared with the CP coatings, the densities of the SHS coatings were significantly enhanced, whose density difference with the theoretical density was reduced from 1.54 to 1.09 g/cm^3 (ZM20), from 1.46 to 1.03 g/cm^3 (ZM30), and from 1.10 to 0.79 g/cm^3 (ZM40), respectively. Due to the increase of density, the oxidation activity of the SHS coating was effectively reduced, and the structural oxygen resistance of the coating in the active oxidation stage was enhanced. The oxygen partial pressure gradient inside the coating led to the appearance of the Si-depleted layer, which critically boosted the complexity of oxygen infiltration. The rise of MoSi_2 content promoted the dispersion of transition metal oxides in SiO_2 , which conduced to shape the homogenous compound glass layer, and enlarged the viscosity of the glass layer. Compared

with SHS-ZM20 and SHS-ZM30 samples, the carbon loss rate of the SHS-ZM40 component was diminished by 76.2% and 66.7%, and the oxygen permeability was decreased by 72.5% and 45.5%, respectively.

Acknowledgements

This work has been supported by the National Natural Science Foundation of China (Nos. 51972338, 51874305, and 51805533), the Fundamental Research Funds for the Central Universities (Nos. 2021ZDPYYQ005 and 2019XKQYMS17), and National Defense Basic Research Program (No. JCKYS2019607004-01). We also appreciate the Advanced Analysis & Computation Center of China University of Mining and Technology.

References

- [1] Hu D, Fu QG, Liu TY, *et al.* Structural design and ablation performance of $\text{ZrB}_2/\text{MoSi}_2$ laminated coating for SiC coated carbon/carbon composites. *J Eur Ceram Soc* 2020, **40**: 212–219.
- [2] Liu GH, Cheng LF, Li KZ, *et al.* Damage behavior of atomic oxygen on zirconium carbide coating modified carbon/carbon composite. *Ceram Int* 2020, **46**: 3324–3331.
- [3] Yan LT, Zhang QJ, Wang JH, *et al.* Effect of ultrasonic vibration on tribological behavior of carbon–carbon composite. *Tribol Int* 2019, **136**: 469–474.
- [4] Liu XS, Fu QG, Wang H, *et al.* Microstructure, thermophysical property and ablation behavior of high thermal conductivity carbon/carbon composites after heat-treatment. *Chinese J Aeronaut* 2020, **33**: 1541–1548.
- [5] Ma QS, Cai LH. Fabrication and oxidation resistance of mullite/yttrium silicate multilayer coatings on C/SiC composites. *J Adv Ceram* 2017, **6**: 360–367.
- [6] Ren XR, Mo HS, Wang WH, *et al.* Ultrahigh temperature ceramic HfB_2 –SiC coating by liquid phase sintering method to protect carbon materials from oxidation. *Mater Chem Phys* 2018, **217**: 504–512.
- [7] Du B, Hong CQ, Qu Q, *et al.* Oxidative protection of a carbon-bonded carbon fiber composite with double-layer coating of MoSi_2 –SiC whisker and TaSi_2 – MoSi_2 –SiC whisker by slurry method. *Ceram Int* 2017, **43**: 9531–9537.
- [8] Liu D, Fu QG, Chu YH. Molten salt synthesis, formation mechanism, and oxidation behavior of nanocrystalline HfB_2 powders. *J Adv Ceram* 2020, **9**: 35–44.
- [9] Ren XR, Shang TQ, Wang WH, *et al.* Dynamic oxidation protective behaviors and mechanisms of HfB_2 –20 wt%SiC composite coating for carbon materials. *J Eur Ceram Soc* 2019, **39**: 1955–1964.
- [10] Guo L, Xin H, Zhang Z, *et al.* Microstructure modification of Y_2O_3 stabilized ZrO_2 thermal barrier coatings by laser glazing and the effects on the hot corrosion resistance. *J Adv Ceram* 2020, **9**: 232–242.

- [11] Li CY, Li GB, Ouyang HB, *et al.* ZrB₂ particles reinforced glass coating for oxidation protection of carbon/carbon composites. *J Adv Ceram* 2019, **8**: 102–111.
- [12] Sonber JK, Suri AK. Synthesis and consolidation of zirconium diboride: Review. *Adv Appl Ceram* 2011, **110**: 321–334.
- [13] Ren XR, Chu HA, Wu KY, *et al.* Effect of the ZrB₂ content on the oxygen blocking ability of ZrB₂–SiC coating at 1973 K. *J Eur Ceram Soc* 2020, **41**: 1059–1070.
- [14] Xue CQ, Zhou HJ, Hu JB, *et al.* Fabrication and microstructure of ZrB₂–ZrC–SiC coatings on C/C composites by reactive melt infiltration using ZrSi₂ alloy. *J Adv Ceram* 2018, **7**: 64–71.
- [15] Ren XR, Lv J, Li W, *et al.* Influence of MoSi₂ on oxidation protective ability of TaB₂–SiC coating in oxygen-containing environments within a broad temperature range. *J Adv Ceram* 2020, **9**: 703–715.
- [16] Grohsmeier RJ, Silvestroni L, Hilmas GE, *et al.* ZrB₂–MoSi₂ ceramics: A comprehensive overview of microstructure and properties relationships. Part I: Processing and microstructure. *J Eur Ceram Soc* 2019, **39**: 1939–1947.
- [17] Gu SC, Zhu SZ, Ma Z, *et al.* Preparation and properties of ZrB₂–MoSi₂–glass composite powders for plasma sprayed high temperature oxidation resistance coating on C/SiC composites. *Powder Technol* 2019, **345**: 544–552.
- [18] Jiang Y, Feng D, Ru HQ, *et al.* Oxidation protective ZrB₂–MoSi₂–SiC–Si coating for graphite materials prepared by slurry dipping and vapor silicon infiltration. *Surf Coat Technol* 2018, **339**: 91–100.
- [19] Yao XY, Li HJ, Zhang YL, *et al.* Oxidation and mechanical properties of SiC/SiC–MoSi₂–ZrB₂ coating for carbon/carbon composites. *J Mater Sci Technol* 2014, **30**: 123–127.
- [20] Zhang WZ, Zeng Y, Gbologah L, *et al.* Preparation and oxidation property of ZrB₂–MoSi₂/SiC coating on carbon/carbon composites. *Trans Nonferrous Met Soc China* 2011, **21**: 1538–1544.
- [21] Ren XR, Shi HL, Wang WH, *et al.* Influence of the ZrB₂ content on the anti-oxidation ability of ZrB₂–SiC coatings in aerobic environments with broad temperature range. *J Eur Ceram Soc* 2020, **40**: 203–211.
- [22] Zhang ML, Ren XR, Chu H, *et al.* Oxidation inhibition behaviors of the HfB₂–SiC–TaSi₂ coating for carbon structural materials at 1700 °C. *Corros Sci* 2020, **177**: 108982.
- [23] Balbo A, Sciti D. Spark plasma sintering and hot pressing of ZrB₂–MoSi₂ ultra-high-temperature ceramics. *Mater Sci Eng: A* 2008, **475**: 108–112.
- [24] Kubota Y, Tanaka H, Arai Y, *et al.* Oxidation behavior of ZrB₂–SiC–ZrC at 1700 °C. *J Eur Ceram Soc* 2017, **37**: 1187–1194.
- [25] Bai YH, Sun MY, Li MX, *et al.* Improved fracture toughness of laminated ZrB₂–SiC–MoSi₂ ceramics using SiC whisker. *Ceram Int* 2018, **44**: 8890–8897.
- [26] Yen BK, Aizawa T, Kihara J, *et al.* Reaction synthesis of refractory disilicides by mechanical alloying and shock reactive synthesis techniques. *Mater Sci Eng: A* 1997, **239–240**: 515–521.
- [27] Vorotilo S, Levashov EA, Kurbatkina VV, *et al.* Self-propagating high-temperature synthesis of nanocomposite ceramics TaSi₂–SiC with hierarchical structure and superior properties. *J Eur Ceram Soc* 2018, **38**: 433–443.
- [28] Iatsyuk IV, Pogozhev YS, Levashov EA, *et al.* Combustion synthesis of high-temperature ZrB₂–SiC ceramics. *J Eur Ceram Soc* 2018, **38**: 2792–2801.
- [29] Jiang ZW, Zhu GM, Feng PZ, *et al.* In situ fabrication and properties of 0.4MoB–0.1SiC–xMoSi₂ composites by self-propagating synthesis and hot-press sintering. *Ceram Int* 2018, **44**: 51–56.
- [30] Peng L, Zhang KB, He ZS, *et al.* Self-propagating high-temperature synthesis of ZrO₂ incorporated Gd₂Ti₂O₇ pyrochlore. *J Adv Ceram* 2018, **7**: 41–49.
- [31] Licheri R, Orrù R, Musa C, *et al.* Combination of SHS and SPS Techniques for fabrication of fully dense ZrB₂–ZrC–SiC composites. *Mater Lett* 2008, **62**: 432–435.
- [32] Varma A, Mukasyan AS. Combustion synthesis of advanced materials: Fundamentals and applications. *Korean J Chem Eng* 2004, **21**: 527–536.
- [33] Vorotilo S, Levashov EA, Petrzhik MI, *et al.* Combustion synthesis of ZrB₂–TaB₂–TaSi₂ ceramics with microgradient grain structure and improved mechanical properties. *Ceram Int* 2019, **45**: 1503–1512.
- [34] Yang Y, Li MS, Xu L, *et al.* Oxidation behaviours of ZrB₂–SiC–MoSi₂ composites at 1800 °C in air with different pressures. *Corros Sci* 2019, **157**: 87–97.
- [35] Silvestroni L, Stricker K, Sciti D, *et al.* Understanding the oxidation behavior of a ZrB₂–MoSi₂ composite at ultra-high temperatures. *Acta Mater* 2018, **151**: 216–228.
- [36] Wang L, Fu QG, Zhao FL. A novel gradient SiC–ZrB₂–MoSi₂ coating for SiC coated C/C composites by supersonic plasma spraying. *Surf Coat Technol* 2017, **313**: 63–72.
- [37] Zou BL, Hui Y, Huang WZ, *et al.* Oxidation protection of carbon/carbon composites with a plasma-sprayed ZrB₂–SiC–Si/Yb₂SiO₅/LaMgAl₁₁O₁₉ coating during thermal cycling. *J Eur Ceram Soc* 2015, **35**: 2017–2025.
- [38] Fahrenholtz WG. Thermodynamic analysis of ZrB₂–SiC oxidation: Formation of a SiC-depleted region. *J Am Ceram Soc* 2007, **90**: 143–148.
- [39] Zhang XH, Hu P, Han JC. Structure evolution of ZrB₂–SiC during the oxidation in air. *J Mater Res* 2008, **23**: 1961–1972.
- [40] Fahrenholtz WG. The ZrB₂ volatility diagram. *J Am Ceram Soc* 2005, **88**: 3509–3512.

Open Access This article is licensed under a Creative Commons Attribution 4.0 International License, which permits use, sharing, adaptation, distribution and reproduction in any medium or format, as long as you give appropriate credit to the original author(s) and the source, provide a link to the Creative Commons licence, and indicate if changes were made.

The images or other third party material in this article are included in the article's Creative Commons licence, unless indicated otherwise in a credit line to the material. If material is not included in the article's Creative Commons licence and your intended use is not permitted by statutory regulation or exceeds the permitted use, you will need to obtain permission directly from the copyright holder.

To view a copy of this licence, visit <http://creativecommons.org/licenses/by/4.0/>.